Voltage-Controlled Reconfigurable Spin-Wave Nanochannels and Logic Devices

Bivas Rana[1,*] and YoshiChika Otani[1,2,†]

[1]Center for Emergent Matter Science, RIKEN, 2-1 Hirosawa, Wako 351-0198, Japan
[2]Institute for Solid State Physics, University of Tokyo, Kashiwa 277-8581, Japan

(Received 23 August 2017; revised manuscript received 29 November 2017; published 30 January 2018)

Propagating spin waves (SWs) promise to be a potential information carrier in future spintronics devices with lower power consumption. Here, we propose reconfigurable nanochannels (NCs) generated by voltage-controlled magnetic anisotropy (VCMA) in an ultrathin ferromagnetic waveguide for SW propagation. Numerical micromagnetic simulations are performed to demonstrate the confinement of magnetostatic forward volumelike spin waves in NCs by VCMA. We demonstrate that the NCs, with a width down to a few tens of a nanometer, can be configured either into a straight or curved structure on an extended SW waveguide. The key advantage is that either a single NC or any combination of a number of NCs can be easily configured by VCMA for simultaneous propagation of SWs either with the same or different wave vectors according to our needs. Furthermore, we demonstrate the logic operation of a voltage-controlled magnonic XNOR and universal NAND gate and propose a voltage-controlled reconfigurable SW switch for the development of a multiplexer and demultiplexer. We find that the NCs and logic devices can even be functioning in the absence of the external-bias magnetic field. These results are a step towards the development of all-voltage-controlled magnonic devices with an ultralow power consumption.

DOI: 10.1103/PhysRevApplied.9.014033

I. INTRODUCTION

The charge degree of freedom of conduction electrons, i.e., charge current, is used to transmit and control information in conventional electronic devices. The computational capabilities of these electronic devices are heading towards the fundamental quantum limit. Moreover, inherent Joule heating also limits further miniaturization of electronic devices. As an alternative approach, the spin degree of freedom, i.e., the spin angular momentum of electrons, may be used for the transmission and processing of information [1–3]. The spin angular momentum can be carried either by the translational motion of conduction electrons, i.e., conduction electron spin current [4,5], or by collective precessional motion of localized magnetic moments [6–8], i.e., spin waves (SWs) [9–12]. The main advantage of SWs is that they can propagate a much longer distance [13,14] as opposed to conduction electron spin current [15,16] without the flow of electrons, reducing energy consumption to a great extent. Quanta of SWs are known as magnons [17,18]. One of the building blocks of these SW-based devices, i.e., magnonic devices, is the waveguide (WG), which is nothing but a thin film, generally made of 3d ferromagnets [19,20], Heusler alloys [21,22], and ferromagnetic insulators [13,23]. SWs can propagate from one physical location to another location along the WGs.

One of the essential tasks for the successful implementation of SWs in future magnonic devices is guiding SWs through nanochannels (NCs) to send then to a desired position. This is generally done by geometrically patterning the WGs either into a stripe [24,25] or wire [26,27]. However, the SW path cannot be further manipulated in this case, which is essential for reprogrammable magnonic devices [28,29]. Another option could be SW confinement through a channel formed by the dc-current-generated local Oersted field, which again requires a continuous supply of energy. Moreover, the SWs cannot be confined within a channel of submicrometer dimension due to the spatial dispersive nature of Oersted fields. Several reports show SW confinement by an internal demagnetizing field [7,25,30,31]. In this case, the SW channels can be moved laterally along the WG by tuning the excitation frequency. Some recent theoretical [32] and experimental reports [33–35] also demonstrate the channeling of causticlike SW beams along well-defined directions in an in-plane magnetized film (i.e., wider WG), where the direction of SW propagation can be controlled by rotating the medium anisotropy by changing the direction of the bias magnetic field. This distinguishable property of causticlike SWs can be used for the development of a magnonic device, such as a reconfigurable SW splitter, by locally applying the inhomogeneous magnetic field [32]. Another alternative method is the confinement of SWs within a domain wall.

*bivas.rana@riken.jp, bivasranaiitd@gmail.com
†yotani@riken.jp

One numerical study [36] shows the possibility of SW confinement within a very specific type of domain wall in a perpendicularly magnetized film. Very recently, it has been experimentally demonstrated [37] that SWs can be guided through a NC formed by magnetic domain walls in an in-plane magnetized film. These NCs are flexible to move across the WG only under the application of the bias magnetic field. In practical magnonic devices [38,39], we need to selectively control a number of closely spaced spin-wave nanochannels (SWNCs) simultaneously, which is very difficult to execute by using all the methods mentioned above. Moreover, the NC with any arbitrary pattern cannot be realized by the above means. An immediate solution to this problem could be recently discovered voltage-controlled magnetic anisotropy (VCMA), which allows us to tune the interfacial perpendicular magnetic anisotropy (PMA) of an ultrathin 3d ferromagnet by voltage, i.e., electric field [19,40–42] without the flow of the charge current. Moreover, the localized nature of VCMA is suitable for nanoscale magnonic devices. In this paper, we show the feasibility of SW confinement in a NC formed by VCMA. The main advantage is that the NCs can be configured into any arbitrary shape according to our requirements.

Several studies have demonstrated the operation of magnonic logic devices based on propagating SWs [24,38,43] through WGs. One of the building blocks of these logic devices is the SW interferometer, where SWs propagating through two or multiple arms of WGs are interfered either physically [44–46] or electronically [20,43]. The Mach-Zehnder interferometer (MZI) [20,45,47] is most commonly used for this purpose. The phases of SWs in two arms of MZI are manipulated, generally by applying local magnetic fields [20], to control the output interference signal. The local magnetic fields are generated by sending current through a wire-shaped conductor [43,45]. This consumes a considerable amount of power due to Joule heating. As these Oersted fields cannot be localized within the submicrometer length scale, Oersted field-controlled MZIs are inappropriate for nanoscale logic devices. Here, we demonstrate the operation of prototype magnonic logic gates (XNOR and NAND) by applying localized VCMA, which does not need the flow of the charge current, unlike previous studies. Moreover, we show the operation of the voltage-controlled SW switch, which can be used to build up the magnonic multiplexer and demultiplexer for logic operations. Our aim is to develop all-voltage-controlled reconfigurable nanoscale magnonic devices with ultralow power consumption.

II. METHODS

We perform numerical simulations by using Object Oriented Micromagnetic Framework (OOMMF) [48] to demonstrate the operation of SWNC and logic devices by applying VCMA. We choose a 1.3-nm ultrathin $Co_{20}Fe_{60}B_{20}$ film with width w (100, 200, and 800 nm) and length L (2 μm) as a model WG for simulation. The material parameters used in the simulations are the following: gyromagnetic ratio $\gamma = 29.4$ GHz/T, exchange stiffness constant $A = 28$ pJ/m, saturation magnetization $M_s = 1.194 \times 10^6$ A/m, interfacial PMA $K_s = 1.55$ mJ/m^2. In the other unit, M_s is equivalent to 1.5 T ($\mu_0 M_s$) magnetic field, whereas K_s is equivalent to 2.0 T ($\mu_0 H_p$) magnetic field, where $\mu_0 H_p = 2\mu_0 K_s/M_s$. This says that the model film has an out-of-plane easy axis of magnetization with a 0.5 T ($\mu_0 H_{\rm eff}$) effective PMA field, where $\mu_0 H_{\rm eff} = \mu_0(H_p - M_s)$. All the above parameters are taken from our previous report [40]. The Gilbert damping parameter α is chosen to be 0.01 for the sake of simplicity. This enables us to demonstrate the functionality of our model devices more clearly as the SW can propagate a sufficiently longer distance before decay. Some test simulations are also performed to check the functionality of the devices with $\alpha = 0.02$, which is the typical value of α for 1.3-nm ultrathin $Co_{20}Fe_{60}B_{20}$ film [49]. We confirm that the device functionality remains the same even with $\alpha = 0.02$. We artificially put a very high damping parameter (0.9) at the ends (within 25 nm from both ends) of the WG to prevent any spurious signal due to the reflections of SWs from the edges. The cell size is chosen to be $2.5 \times 2.5 \times 1.3$ nm^3, smaller than the exchange length (~5.6 nm) to incorporate the role of exchange interactions on the SW dispersion character.

Previous reports [19,40,50,51] show that PMA energy (K_s) changes linearly with the applied electric field (E), i.e., $\Delta K_s = \beta E$, where β is known as a magnetoelectric coefficient. The value of β can be up to 108 fJ/Vm for the $Co_{20}Fe_{60}B_{20}$/MgO interface [52–54]. This coefficient can be increased further by engineering the interface of MgO with ferromagnetic materials. For instance, β can be up to 140 fJ/Vm for Fe/Pt/MgO [55], 180 fJ/Vm for Fe/MgO [56], 370 fJ/Vm for Cr/Fe/MgO [57], and 602 fJ/Vm for the FePd/MgO interface [58] at room temperature. In our previous report [40], we have shown that the β can be 40 fJ/Vm (i.e., 26 mT/V) and 197 fJ/Vm (127 mT/V) at the $Co_{20}Fe_{60}B_{20}$/MgO interface for positive and negative bias voltages, respectively. Here, the positive bias voltage means the electrode, on top of insulating layer, has a positive potential with respect to the bottom electrode, i.e., WG. For the sake of simplicity, in our micromagnetic simulation we choose β as 155 fJ/Vm (100 mT/V), which is an intermediate value of 40 and 197 fJ/Vm. Moreover, we assume that positive E reduces PMA and negative E induces PMA with the same magnitude of β. In other words, this means an equivalent change of ± 200 mT PMA field ($\mu_0 H_p$) under the application of the electric field $E = \mp 1$ V/nm. Here, we would like to mention that choosing a different value of β for different sign of E can only change the quantitative value of ΔK_s, although the key findings of our study remain unaffected. At first, the ground states of magnetization are prepared by applying a

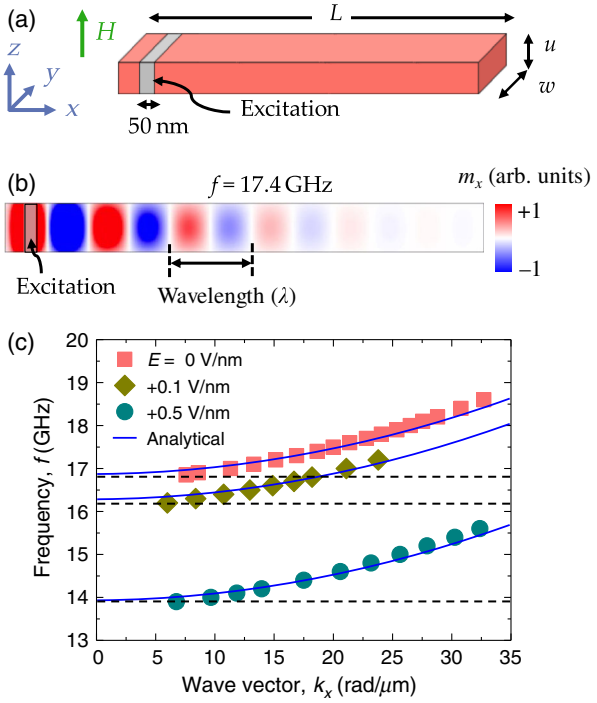

FIG. 1. (a) Schematic illustration of a WG with the dimensions of 2 μm(L) × 200 nm(w) × 1.3 nm(u) is shown. The bias magnetic field of 50 mT is applied along the out-of-plane direction. The SWs are excited by applying a spatially uniform magnetic field on the $50 \times w$ nm^2 area at a distance of 100 nm from the left edge of WG. (b) A typical spatial map of propagating SW with $f = 17.4$ GHz is shown. The rectangular shaded area denotes the area for excitation. The SW wavelength (λ) is marked on the spatial map. (c) Simulated frequency dispersion of SWs as a function of the wave vector (k_x) is represented for three different values of the applied dc electric field (E) at the interface of the SW waveguide. Solid lines represent analytical curves, plotted by using Eq. (1), for three values of applied E. Dotted horizontal lines represent the frequencies that correspond to uniform ferromagnetic resonance.

large-enough magnetic field (5.0 T) along the perpendicular direction for 4 ns to fully saturate the magnetization. The magnetic field is then slowly reduced down to the bias magnetic field value for 4 ns followed by a further relaxation for another 4 ns in the presence of the constant bias magnetic field ($\mu_0 H$). The value of α is chosen to be 0.9 during the preparation of the ground state of magnetization in order to fully relax the system within the given simulation time limit. The SWs are then excited by applying a Gaussian-shaped pulsed magnetic field in the time domain given by $h_y(t) = A_0 \exp[(t - t_0)^2/2\tau^2]$, where A_0, t_0, and τ are constants, which decide the peak amplitude, peak position, and pulse duration, respectively. We choose the pulsed magnetic field of 0.6-mT amplitude, 25-ps pulse duration, and apply it on the $50 \times w$ nm^2 area at a 100-nm distance from the left edge of the WG [Fig. 1(a)]. The pulsed-field amplitude is chosen to be uniform over the $50 \times w$ nm^2 area so that it can excite SWs up to $k_x = 2\pi/0.05 = 125$ rad/μm [59], where k_x is the SW wave vector along the x axis. The excited SW frequencies (f) are extracted by performing a fast Fourier transform of the time-varying SW signals. Next, we apply a time-varying sinusoidal magnetic field along the y axis given by $h_y(t) = A_1 \sin 2\pi f t$, where A_1 is the peak amplitude of the sinusoidal field, f equals to the SW frequency. We choose $A_1 = 0.6$ mT, small enough to excite SWs in the linear regime. This sinusoidal field continuously excites the SWs with a particular SW wave vector (k_x) determined by the SW dispersion character [Eq. (1)].

III. RESULTS

We start with a WG with $w = 200$ nm and $L = 2$ μm. Figure 1(a) shows the schematic illustration of the WG. A bias magnetic field ($\mu_0 H$) of 50 mT is applied along the out-of-plane direction (z axis). In this configuration, the magnetization is aligned perpendicular to the film plane. The SWs are excited by locally applying the sinusoidal magnetic field with a 0.6-mT amplitude (A_1) as discussed in the method section. It excites the magnetostatic forward volumelike spin waves (MSFVWs), which propagate along the long axis (x axis) of WG. There are several advantages of choosing the out-of-plane orientation of magnetization and MSFVW. First of all, MSFVW shows the isotropic frequency dispersion with the wave vector (k) for any arbitrary propagation direction along the film surface. Therefore, the SW frequency and character remain unchanged with the propagation direction. This enables us to investigate the effect only imposed by VCMA. Second, when two or more propagating SWs in an in-plane magnetized film are combined or overlapped, the SWs may show parasitic scattering processes into the higher-order dipolar SW modes and exchange SW modes due to their anisotropic dispersion nature. This problem can be overcome by using the isotropic MSFVW [46]. Third, strong PMA forces the alignment of magnetization along the out-of-plane direction even after removing the bias magnetic field. This enables us to operate SW devices even in the absence of the bias magnetic field. Figure 1(b) represents the snapshot of dynamic magnetization for a propagating MSFVW excited at $f = 17.4$ GHz and $E = 0$, i.e., $\mu_0 H_p = 2$ T. The color code (red-white-blue) represents the x component of dynamic magnetization (m_x). The SW wavelength (λ) determined from this spatial map of dynamic magnetization is about 340 nm, which gives $k_x = 2\pi/\lambda = 18.48$ rad/μm. We excite SWs for different values of f and determine corresponding values of k_x from simulated spatial maps of dynamic magnetization. Figure 1(c) shows the simulated frequency (f) dispersion of SWs as a function of k_x for $E = 0$, i.e., for $\mu_0 H_p = 2$ T. Note that the simulated dispersion curve looks like the parabolic function of k_x. This means the SWs are dominated by the exchange interaction as the SW wavelength (λ) is within only a few hundred nanometers. Therefore, we

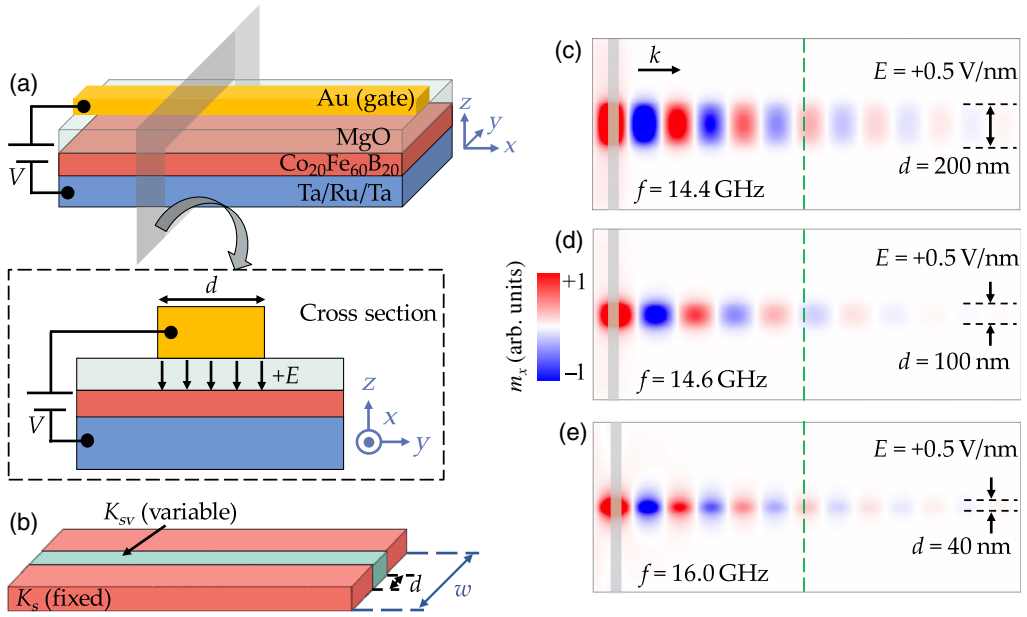

FIG. 2. (a) Schematic diagram of a practical SW device for the confinement of propagating SWs within a NC formed by VCMA. The voltage is applied across the top metal gate electrode and WG. The inset figure represents the cross section of the WG including the direction of the electric field and the lateral position where the electric field is applied. (b) Schematic diagram of the SW device for the micromagnetic simulation to show SW confinement. (c),(d),(e) Simulated spatial maps of dynamic magnetization demonstrate the SW confinement in 200, 100, and 40 nm straight channels, respectively, formed by applying a +0.5 V/nm electric field through the top gate electrode as shown in Fig. 2(a). Rectangular gray shaded parts represent the area where the sinusoidal magnetic field is applied for the SW excitations.

call these SWs as exchange-dominated MSFVWs. Now, if we apply positive E at the interface of WG, it will reduce PMA (K_s) and downshift the dispersion curves as depicted in Fig. 1(c) for $E = +0.1$ V/nm and $+0.5$ V/nm. In practice, it can be done by placing a top metal gate electrode on the WG and applying voltage across the top gate electrode and WG (i.e., bottom electrode) [60]. The dotted horizontal lines represent the frequencies that correspond to a uniform ferromagnetic resonance (UFMR) for the corresponding three different values of E, i.e., K_s. Theoretically, the exchange-dominated MSFVWs in an ultrathin film with PMA can be described by the following analytical expression [61,62]:

$$f = \frac{\gamma\mu_0}{2\pi}\left\{\left(H + \frac{2A}{\mu_0 M_s}k^2 + H_p(E) + (N_y - N_z)M_s\right)\right.$$
$$\times\left[H + \frac{2A}{\mu_0 M_s}k^2 + H_p(E)\right.$$
$$\left.\left.+ (N_x - N_z)M_s\left(\frac{1 - e^{-ku}}{ku}\right)\right]\right\}^{1/2}. \quad (1)$$

Here, N_x, N_y, and N_z are the demagnetizing factors along the x, y, and z axis, respectively, which satisfy the condition of $N_x + N_y + N_z = 1$. For infinite thin film, $N_x = N_y = 0$ and $N_z = 1$. However, in a confined thin film, i.e., WG, the values of the demagnetizing factors can be different [63,64]. The second term inside the first bracket includes the contribution from the exchange interaction, whereas the third term includes the electric-field-dependent interfacial PMA field. In Fig. 1(c), we also plot the theoretical dispersion curves (solid lines) for different values of E, i.e., K_s. We can see that the theoretical curves nicely reproduce the simulation results.

Next, we show the SW confinement through a NC. We consider a 1.3-nm ultrathin WG ($Co_{20}Fe_{60}B_{20}$ film) with $w = 800$ nm, $L = 2$ μm, and $K_s = 1.55$ mJ/m^2. Our aim is to confine SWs in a NC with a width d (where $d < w$) and length L. For this purpose, a positive E is applied on the $d \times L$ surface area of WG through a top metal gate electrode with the same dimension ($d \times L$) as shown in Fig. 2(a) and the inset. This positive E reduces the PMA of this area by $\Delta K_s = \beta E$ and creates a sharp rectangular potential well of the $d \times L$ area with ΔK_s depth, where the SW dispersion curve is downshifted with respect to the rest of the area of WG. For instance, the dispersion curve underneath the gate electrode can be downshifted by 3 and 0.65 GHz by applying $E = +0.5$ and $+0.1$ V/nm, respectively, as shown in Fig. 1(c). In this situation, if a sinusoidal magnetic field is applied with the frequency (f), which only satisfies the SW resonance condition for the WG with a positive E but remains well below the bottom frequency of the dispersion curve for the WG with $E = 0$ V/nm, SWs are only excited and propagated through the channel underneath the top gate electrode. This is because the SWs with this f are forbidden outside the area underneath the gate electrode. To realize this in simulation, we keep K_s

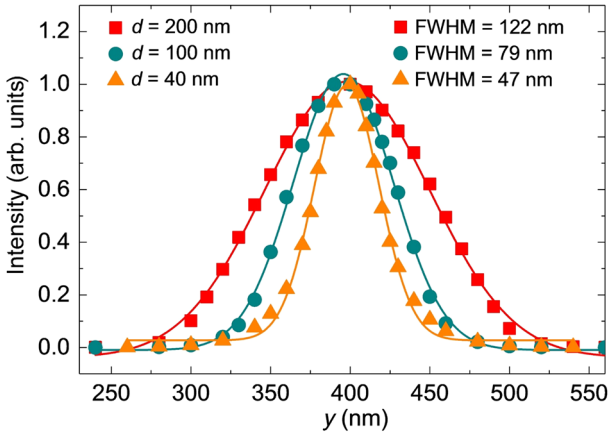

FIG. 3. Line scans of SW intensity as a function of y at $x = 1$ μm are shown for three different widths of NC. The line scans are taken across the dotted lines shown in Figs. 2(c), 2(d), and 2(e). The solid lines show the fitting of these data with a Gaussian function to determine the FWHM.

fixed to 1.55 mJ/m^2, where $E = 0$ (i.e., outside the gate electrode) and replace K_s by $K_{sv}(= K_s + \beta E)$, where the positive E is applied as schematically depicted in Fig. 2(b). However, all the other magnetic parameters such as γ, A, and M_s are kept constant throughout the WG. At first, we would like to show the SW confinement within the 200-nm straight channel by applying $E = +0.5$ V/nm. Figure 2(c) represents the simulated spatial map of dynamic magnetization which shows the confinement of SW with $f =$ 14.4 GHz through a 200 nm straight channel. Here, we arbitrarily choose $f = 14.4$ GHz, as this satisfies the SW dispersion condition for $E = +0.5$ V/nm and well below $f = 16.85$ GHz, i.e., the bottom of the dispersion curve for $E = 0$ V/nm [Fig. 1(c)]. In fact, we can choose any frequency in the range of 13.9 GHz $< f <$ 16.85 GHz, where 13.9 and 16.85 GHz are the UFMR frequency of the WG for $E = +0.5$ and $E = 0$ V/nm, respectively. The width of the NC can be further reduced by decreasing the width (d) of the top-gate electrode. Now, we use two different top-gate electrodes with $d = 100$ and 40 nm to form NC with lower widths. Figures 2(d) and 2(e) show the SW confinement in 100 and 40 nm NC, respectively. This proves that the SWs can be confined within a NC down to few tens of nanometer by VCMA.

To further confirm whether SWs are really confined within the NCs, we perform a line scan along the dotted vertical lines shown in Figs. 2(c), 2(d), and 2(e). In Fig. 3, we plot the line scan of simulated SW intensity as a function of y at $x = 1$ μm. The solid lines represent the fitting with a Gaussian function. The results show that the full width at half maxima (FWHM) of the fitted curves are 122, 79, and 47 nm for NCs with $d = 200$, 100, and 40 nm, respectively. This tells us that the SWs are strongly confined within the NCs with the width down to 40 nm formed by VCMA.

Note that 40 nm is not the lower limit of the NC width (d) for the SW confinement. In general, the SW frequency f increases with the decrease of d [65] due to a variation of the demagnetizing factors with the WG (i.e., NC) dimension [63,64]. Therefore, if the d is further reduced below 40 nm, the SW frequency in NC formed by $E = +0.5$ V/nm becomes almost equal to the SW frequency outside of NC (see Appendix A). As a result, SWs cannot be confined within the NC with $d < 40$ nm by applying $E = +0.5$ V/nm. However, if positive E is increased above $+0.5$ V/nm or if β is increased beyond 155 fJ/Vm (which is possible according to previous reports [56–58]), SWs may be confined even in a NC with $d < 40$ nm. Furthermore, the SWs can be confined even by applying the positive E, lower than $+0.5$ V/nm with $\beta = 155$ fJ/Vm. To confirm this we also run some simulations to show the SW confinement through a 200-nm channel by applying $E = +0.1$ V/nm. In Appendix B, we represent the simulated spatial map and corresponding line scan, which confirms that the SWs can be confined within the 200-nm channel even by applying $E = +0.1$ V/nm. We again mention here that this is not the fundamental lower limit of E for the SW confinement. SWs can be confined even by applying the lower value of positive E if a material system with a higher value of β (i.e., $\beta >$ 155 fJ/V m) is chosen. This is because the SWs are confined within the NC formed by a potential well of ΔK_s depth, where ΔK_s can be controlled by β and E. This encourages further study to find out material systems with higher values of β to reduce power consumption of the future spintronics devices.

For a successful implementation of SWs in future magnonic devices, it is necessary to send SWs along bended or curved channels. Magnetostatic spin waves are generally anisotropic for in-plane orientation of magnetization. As a result, SWs cannot propagate efficiently beyond a curved path. Therefore, we have used isotropic MSFVW dominated by exchange interaction. Now, we would like to see whether these isotropic SWs can propagate through a curved NC formed by VCMA. Figure 4(a) represents the schematic of a WG with a single curved NC of width $d = 100$ nm. In practice, this kind of curved NC can be created by designing the top gate electrode with the same shape as that of the NC and by applying dc voltage across the top gate electrode and WG. In Fig. 4(d), the simulation result shows that SWs can propagate even through a curved NC formed by VCMA. Figures 4(b) and 4(c) represent the schematic diagram of two more WGs where a single straight NC is divided into two symmetric branches of NCs. The snapshots of dynamic magnetization, as represented in Figs. 4(e) and 4(f), show that SWs are also divided into two parts and propagated through two branches of NCs. Figures 4(e) and 4(f) are typical examples of the SW divider or splitter, which can split an incoming SW into two or more propagating SWs. This means that SW splitters can be integrated on an

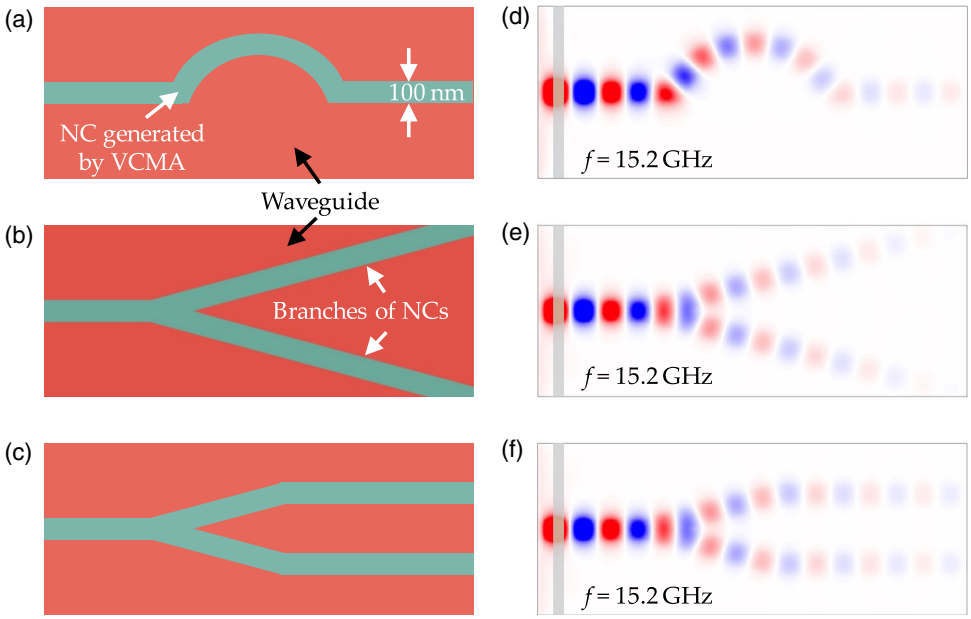

FIG. 4. (a),(b),(c) Schematic diagrams show the top view of the WGs with the dimensions of $2\mu\text{m}(L)\times 800\text{nm}(w)\times 1.3\text{nm}(u)$. NCs ($d = 100$ nm) with three different shapes are formed by designing the top gate electrode. Part (a) represents a single straight NC with curved structure, whereas parts (b) and (c) represent the division of a single NC into two symmetric branches. (d),(e),(f) Snapshots of dynamic magnetization show the SW ($f = 15.2$ GHz) confinement in those NCs with different shapes.

extended WG by VCMA. Likewise, the SW combiner which combines two or more SWs, can also be formed by VCMA. These SW splitters and combiners are the essential components of a SW interferometers or logic devices.

Figure 5 represents one of the key points of this paper. Here, we consider a WG with $w = 800$ nm and $L = 2$ μm. Figure 5(a) shows that three NCs with $d = 100$ nm separated by 150 nm are formed by VCMA via three electrically isolated metal gate electrodes (not shown). At first, channel 1 is switched on by applying $E = +0.5$ V/nm across the top gate electrode (no. 1) and the WG. Figure 5(b) shows that although the SW is excited across the whole width of the WG, it is only confined within channel 1. Likewise, SWs can also be confined either within channel 2 or channel 3 by selectively applying E across the corresponding top gate electrode and WG as represented in Figs. 5(c) and 5(d), respectively. Figure 5(e) says that three NCs can also be selected simultaneously for

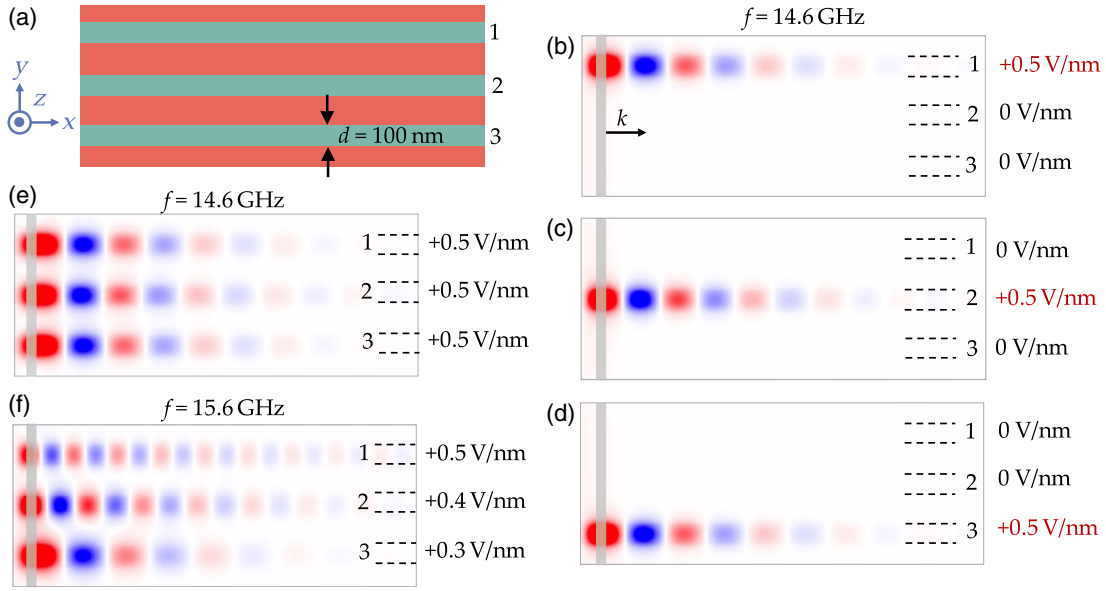

FIG. 5. (a) Schematic diagram show top view of WG with the dimensions of 2 μm(L) × 800 nm(w) × 1.3 nm(u). Three parallel NCs (1, 2, 3) with $d = 100$ nm are formed by applying VCMA via three electrically isolated metal gate electrodes (not shown). (b),(c),(d) Spatial maps of dynamic magnetization show that any NC can be selected for sending SWs by applying the electric field E corresponding to the top gate electrode of that NC. (e),(f) Spatial maps of dynamic magnetization show that SWs in different NCs can be simultaneously sent and configured either with the same wavelength (λ), i.e., wave vector (k_x) or with different λ, i.e., k_x by VCMA.

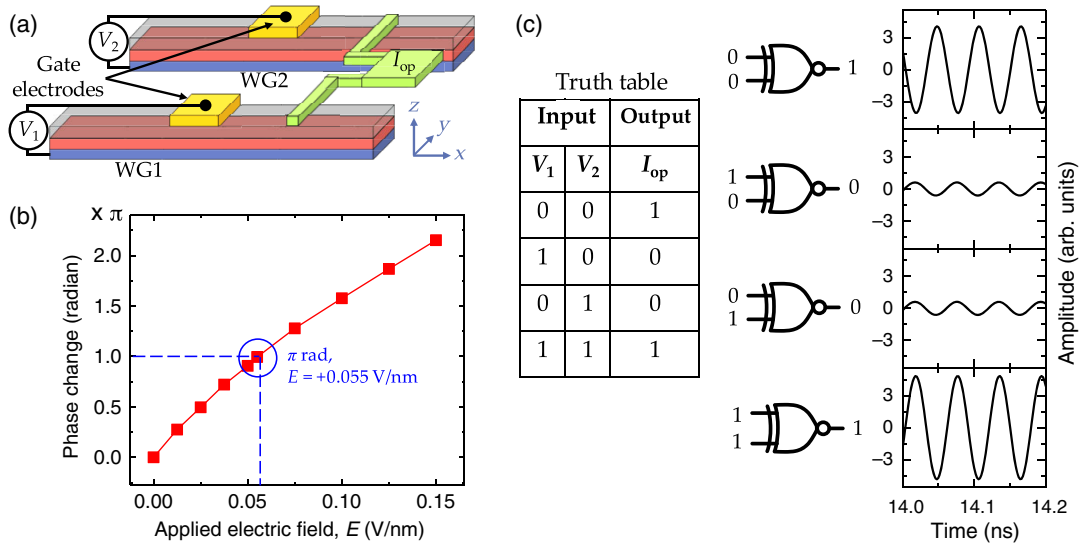

FIG. 6. (a) Schematic diagram shows the device structure of a voltage-controlled XNOR gate consists of two parallel WGs (WG1 and WG2) with the dimensions of 2 μm$(L) \times 200$ nm$(w) \times 1.3$ nm(u). Two metal gate electrodes with the dimensions of 300 nm $\times$ 200 nm are placed on each WG at $x = 700$ nm for controlling the phase of propagating spin wave. The output electronic signal (I_{op}) of the SW interference is collected from $x = 1$ μm. (b) The graph shows the change in the accumulated SW phase with an applied electric field (E). The solid circle indicates the data point corresponds to the change in the π phase by applying $E = +0.055$ V/nm. (c) Simulated results represent the operation of a XNOR gate. Here, we show the electronic interference signals for different combinations of input voltages. The truth table is also shown on the left-hand side.

sending SWs with the same wave vector k_x. Here, $E = +0.5$ V/nm is applied across all the top gate electrodes and WG. In Appendix C, we present some more results on this, where we show that SWs can be sent through any combination of NCs. This means one can selectively send SWs through any NC or any combination of NCs by applying VCMA. Now, we would like to see whether or not SWs with different wave vectors can be sent simultaneously through different NCs. For this purpose, three NCs (1, 2, 3) are formed by applying $E = +0.5$ V/nm, $+0.4$ V/nm, $+0.3$ V/nm, respectively, and SWs with the same frequency f (15.6 GHz) are sent through all these NCs. Here, $f = 15.6$ GHz is chosen as it satisfies the SW resonance condition for all the NCs created under the application of the aforementioned electric fields. In Fig. 5(f) we represent the spatial map of dynamic magnetization, which shows that SWs with different wave vectors are propagating through different NCs formed by applying different values of E in different NCs. Here, SWs (same frequency) with different wave vectors are excited due to different values of PMA in different NCs according to Eq. (1). These results clearly show that the NCs can be reconfigured by VCMA according to our needs. Here, we would like to mention that parallel NCs (more than one) with hundreds of nanometer separations are very difficult to create by magnetic domain walls. Even though they are created, it is not possible to selectively send SWs with either the same or different wave vectors through a NC or combination of NCs. This is one of the key advantages of voltage-controlled NCs over that of the NCs formed by magnetic domain walls or by other means.

Now, we will demonstrate the operation of voltage-controlled magnonic logic devices. One of the building blocks of logic devices is the interferometer. MZIs are most commonly used for this purpose. Here, we show the function of a voltage-controlled prototype XNOR logic gate based on MZI. Figure 6(a) represents the schematic diagram of the interferometer composed of two parallel geometrically structured WGs with $w = 200$ nm, $L = 2$ μm, and a 200-nm edge-to-edge distance. The separation between the WGs is chosen to be the same as their width to avoid dynamic magnetostatic coupling between them. These two WGs play the role of the arms in a MZI. The SWs with $f = 17.1$ GHz are simultaneously excited in two WGs at a distance of 100 nm from the left edge as discussed in the method section. This means that the excited SWs should have the same initial phase. A metal gate electrode with a dimension of 300 nm$(x) \times$ 200 nm(y) is placed on each WG at a distance of 700 nm from its left edge. When positive E is applied at the interface of the WG through the gate electrodes, the SW dispersion curve of the WG underneath the gate electrode is downshifted as shown in Fig 1(c). In other words, the wave vector of the SWs propagating underneath the gate electrode increases due to the application of positive E (see Appendix D). The phase accumulation by a propagating SW can be written by a simple formula given by the following: accumulated phase = wave vector $(k) \times$ distance traveled. Therefore, SWs accumulate more phase after passing through the gate electrodes with a positive E. Figure 6(b) shows that the change in the accumulated phase

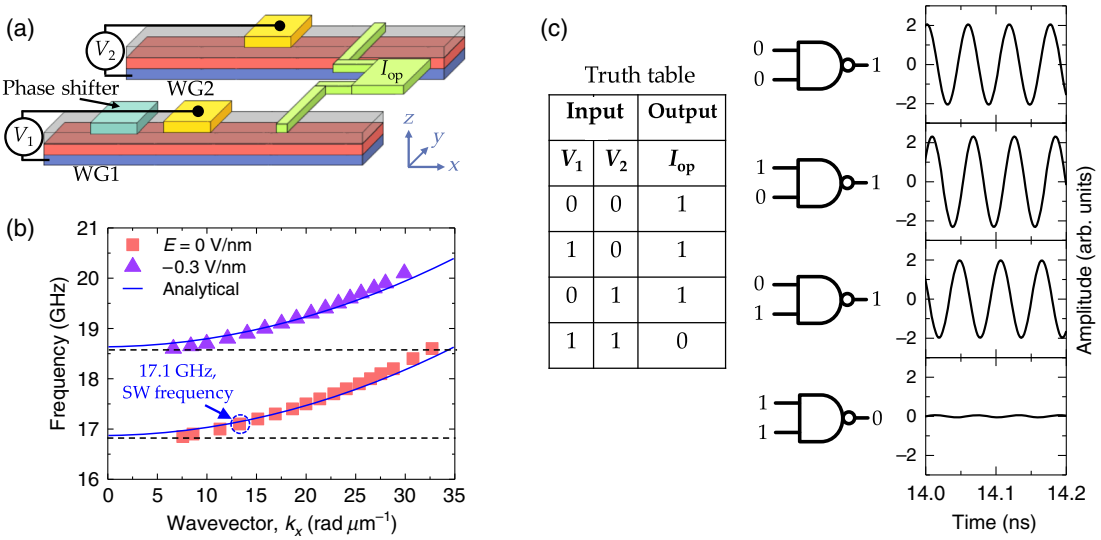

FIG. 7. (a) Schematic diagram shows the device structure of a voltage-controlled universal NAND gate consists of two parallel WGs (WG1 and WG2) with the dimensions of 2 μm(L) × 200 nm(w) × 1.3 nm(u). Two metal gate electrodes with the dimensions of 300 nm × 200 nm are placed on each WG at $x = 700$ nm for controlling propagating SWs. A phase shifter with the dimensions of 300 nm × 200 nm is also put on top of WG1 at $x = 300$ nm for adding the $2\pi/3$ phase to the SWs in WG1. (b) The frequency dispersion of SWs is plotted as a function of the wave vector k_x for two values of applied electric fields (E). The dotted circle represents the excited SW frequency (17.1 GHz). Solid lines represent analytical curves [Eq. (1)] for two values of E. (c) Simulated results represent the operation of a voltage-controlled universal NAND gate. Here, we show the electronic interference signals for different combinations of input voltages. The truth table is also shown on the left-hand side.

increases monotonically with an applied positive E. The accumulated phase of the SWs increases by π and 2π when applied E becomes $+0.055$ V/nm and $+0.137$ V/nm, respectively. To show the function of the prototype MZI, the SW signals (at $x = 1.5$ μm) from both WGs are interfered electronically. In practice, the time-varying SW signal at $x = 1.5$ μm may be read electronically by using a magnetic tunnel junction. A thin magnetic layer with an in-plane easy axis of magnetization, placed on top of the oxide (MgO) layer can be used as the reference layer, whereas the WG can serve as the free layer. In the MZI, the applied gate voltages V_1, V_2 on two WGs are used as logic inputs, whereas the amplitude of the electrical interference signal (I_{op}) is used as logic output. Logic input "0" represents the situation when the applied voltage $V = 0$ and the logic input "1" represents the situation when the applied voltage V creates an electric field $E = +0.055$ V/nm to induce an accumulated SW phase of π. Destructive interference, i.e., the minimum interference signal, represents the logic output 0, whereas constructive interference, i.e., the maximum interference signal, represents the logic output 1. Figure 6(c) represents the output interference signals for different combinations of input voltages. The output shows very large constructive interference signals either for $V_1 = V_2 = 0$ or for $V_1 = V_2 = 1$. This is because the SWs in two arms of the interferometer accumulate the same phase after passing through the gate electrodes. We call this logic output 1. On the other hand, the output shows much smaller destructive interference signals either for $V_1 = 0$, $V_2 = 1$ or for $V_1 = 1$, $V_2 = 0$ as the SWs in two arms of the interferometer become out of phase after passing through gate electrodes. This represents the logic output 0. The truth table of the MZI, as shown in Fig. 6(c), resembles the XNOR gate. We would like to mention that the I_{op} for $V_1 = V_2 = 0$ does not match the I_{op} for $V_1 = V_2 = 1$. Moreover, the I_{op} does not become zero or negligibly small for the destructive interference, i.e., for the logic output 0. The above situation is likely to happen only if the amplitudes of two interfering SWs are different. Here, the reason behind this unequal SW amplitude is the difference in the SW decay lengths in two arms of MZI imposed by VCMA (see Appendix E for details).

We also propose and demonstrate the operation of a voltage-controlled prototype universal NAND gate by using a similar kind of MZI as used for the XNOR gate. The schematic diagram of the MZI for the NAND gate is represented in Fig. 7(a). The only difference is that we use an additional phase shifter to add the $2\pi/3$ phase to the SW in WG1 with respect to the SW in WG2. The phase shifter is nothing but an additional metal gate electrode with an area of 300 nm × 200 nm. A dc electric field of $+0.094$ V/nm is applied at the interface of WG1 through the gate electrode of the phase shifter to shift the SW phase of WG1 by $+2\pi/3$ with respect to the SW phase in WG2. The phase shifter is used so that the output SW interference signals have almost similar amplitudes in case of logic 1 for different combinations of inputs, as discussed in Ref. [43]. The gate voltages V_1, V_2 on two WGs are used as logic

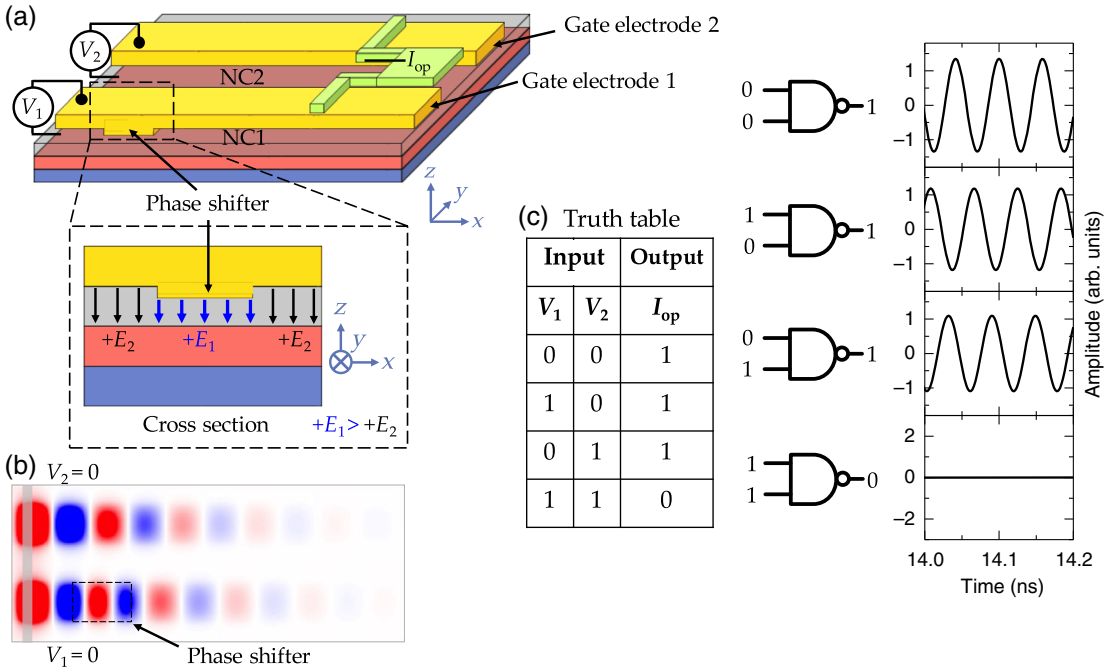

FIG. 8. (a) Schematic diagram shows the device structure of a voltage-controlled universal NAND gate consists of two parallel NCs (NC1 and NC2) with the dimensions of 2 μm $(L) \times 200$ nm (d), formed by applying the voltage through the two top gate electrodes. A phase shifter with the dimensions of 300 nm $\times$ 200 nm is formed on top of NC1 at $x = 300$ nm for adding the $2\pi/3$ phase to the SWs in NC1 with respect to the SWs in NC2. This phase shifter is designed by reducing the thickness of the dielectric layer in the 300 nm $\times$ 200 nm rectangular area by physical ion etching before depositing gate electrodes. (b) The spatial map of dynamic magnetization shows the propagation of SWs through two parallel voltage-controlled NCs for $V_1 = V_2 = 0$. (c) Simulated results represent the operation of an all-voltage-controlled universal NAND gate. Here, we show the electronic interference signals for different combinations of input voltages. The truth table is also shown on the left-hand side.

inputs similar to the XNOR gate. This time V_1, V_2 are chosen to be negative to apply $E = -0.3$ V/nm for logic the input 1. The negative gate voltage locally induces the PMA to shift the SW dispersion curve in the upward direction as shown in Fig. 7(b). This induces a square-shaped potential step where propagating SWs with a given frequency (here we use 17.1 GHz) is forbidden. As a result, SWs cannot propagate beyond the area underneath the top gate electrodes for logic input 1. Therefore, these gate electrodes act like switches. Figure 7(c) shows the output interference signals for different combinations of logic inputs. When logic inputs are 0, i.e., $V_1 = V_2 = 0$, SWs can pass through the gates freely and generate a large SW interference signal (logic output 1). Similar kinds of interference signals are also obtained when one of the logic inputs is 0 and another one is 1. When both logic inputs are 1, SWs in both arms of the MZI are blocked by gate electrodes and produce a negligibly small interference signal (logic output 0). The truth table of logic operation, as shown in Fig. 7(c), resembles the universal NAND gate.

In principle, voltage-controlled SWNC and magnonic logic devices (e.g., the NAND gate) can be realized in a single device. In Fig. 8, we represent the schematic diagram of the proposed device. For this, we consider a WG with a dimension of 2 μm$(L) \times 800$ nm$(w) \times 1.3$ nm(u). In this particular case, we consider that the WG has a PMA field $(\mu_0 H_p)$ of 2.1 T. Two NCs are formed by placing two metal gate electrodes of dimension 2 μm $\times$ 200 nm and an edge-to-edge separation of 200 nm on top of the WG and applying voltage across the gate electrodes and WG. We have already discussed that a phase shifter in NC1 is necessary for the operation of the universal NAND gate. This can be fabricated by reducing the thickness of the insulating oxide layer (above the ferromagnetic layer) on the 300 nm $\times$ 200 nm rectangular area at a distance of 300 nm from the left side of the WG by lithography and physical ion etching prior to the fabrication of gate electrodes. This enables us to apply a relatively higher electric field (E_1) on the rectangular area as compared to the electric field (E_2) on the rest of the area underneath the gate electrodes. For instance, the thickness of the oxide layer in the rectangular area should be chosen in such a way that an electric field $E = +(0.5 + 0.094)$ V/nm is applied on it, whereas $E = +0.5$ V/nm is applied on the rest of the area. Here, logic input 1 represents the situation when the applied voltage $V = 0$ and the logic input 0 represents the situation when the applied voltage V creates the electric field $E = +0.5$ V/nm$(+0594$ V/nm$)$ underneath the gate electrodes

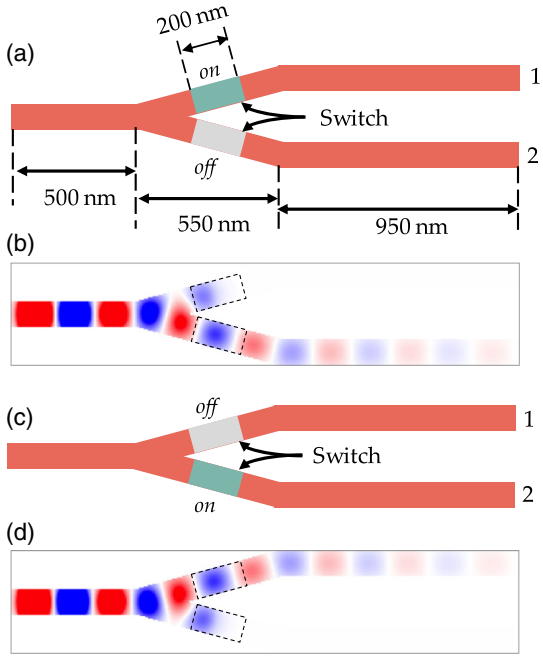

FIG. 9. (a),(c) Schematic diagrams show the device structure of a voltage-controlled SW switch. The device consists of a WG with a width $w = 100$ nm, which is divided into two symmetric branches (1 and 2) of the same widths at a distance of 500 nm from the left edge of the WG. Two metal gate electrodes with the dimensions of 200 nm × 100 nm are placed on top of two branches for the switching operation. (b),(d) Images of the simulated spatial maps of dynamic magnetization show that the SW can be switched in between WG1 and WG2 by selectively turning "*on*" and "*off*" the switches placed on WG1 and WG2.

(rectangular area). The large interference signal represents the logic output 1, while the small interference signal represents the logic output 0. Figure 8(b) represents the snapshot of the spatial distribution of dynamic magnetization for $V_1 = V_2 = 0$. It shows that the SWs with the same initial phase propagate through two NCs. A phase difference of $2\pi/3$ is introduced between these SWs when SW in NC1 crosses through the phase shifter. The interference signals for four different input compositions are shown in Fig. 8(c). The output shows the minimum interference signal only when $V_1 = V_2 = 1$. In this particular case, the NCs are not formed, as no gate voltage is applied. As a result, SWs cannot propagate through the WG and show the 0 output signal. For the other three combinations of inputs, either one of the NCs or both NCs are formed for the propagation of SWs and produce a maximum interference signal, i.e., logic output 1. The truth table, as shown in Fig. 8(c), resembles the universal NAND gate.

In the last part, we demonstrate the operation of a voltage-controlled SW switch. Figures 9(a) and 9(c) show the schematic diagram of the switching device. It consists of a geometrically structured WG, which is divided into two symmetric branches (branch 1 and branch 2), keeping the width (100 nm) same throughout the WG length. The SWs with $f = 18.2$ GHz are excited at a distance of 100 nm from the left edge of the WG. After a propagation of about 400 nm, the SWs are divided into two equal parts and propagate freely along the two branches (not shown). For switching operation, we put two voltage-controlled switches with an area of 200 nm × 100 nm on two branches, as shown in Figs. 9(a) and 9(c). SW switches are nothing but metal gate electrodes, as discussed in the above section (see universal NAND gate). When a negative voltage is applied to the switches (i.e., switches are "*on*") for generating the electric field $E = -0.3\text{V/nm}$ at the surface of WG, SWs cannot propagate beyond the switches. SWs are allowed to propagate only when switches are "*off*". Figures 9(b) and (9d) show that the SWs can be switched in between channels 1 and 2 by selectively putting the switches of two WGs in the *on* and *off* mode by applying VCMA. Here, we have considered a simple and basic structure of WG for the switching operation. However, the switching operation by VCMA is also possible for the complex structure of the WG with a number of symmetric or asymmetric branches. The operation principle of this SW switch resembles the SW demultiplexer, where the SW signal from a single input line can be transferred to one of the several output lines. Likewise, a SW multiplexer may also be constructed by using SW switches, where SW signal from one of the several input lines is transferred to a single output line.

IV. CONCLUSIONS

In conclusion, we propose voltage-controlled reconfigurable NCs with a width down to a few tens of nanometers for SW propagation. We use numerical micromagnetic simulation to show the confinement of exchange-dominated isotropic magnetostatic forward volumelike SWs (MSFVW) in the NCs. The NCs can be designed either into a straight or curved structure, depending on the design of the top gate electrode. We show various reconfigurable properties of these NCs. The key advantage is that a number of closely spaced NCs can be configured on an extended WG by VCMA for sending SWs either with the same or different wave vectors in different NCs. Furthermore, we propose and demonstrate the operation of the voltage-controlled magnonic XNOR gate, universal NAND gate, and SW switch. We also propose a device to realize both the voltage-reconfigurable SWNCs and voltage-controlled magnonic logic devices together in one device. This universal NAND gate can be used to construct other logic gates. As electric fields can be confined within the nanometer length scale, these voltage-controlled NCs, logic devices, and switches can be further scaled down to develop high-density nanoscale magnonic devices.

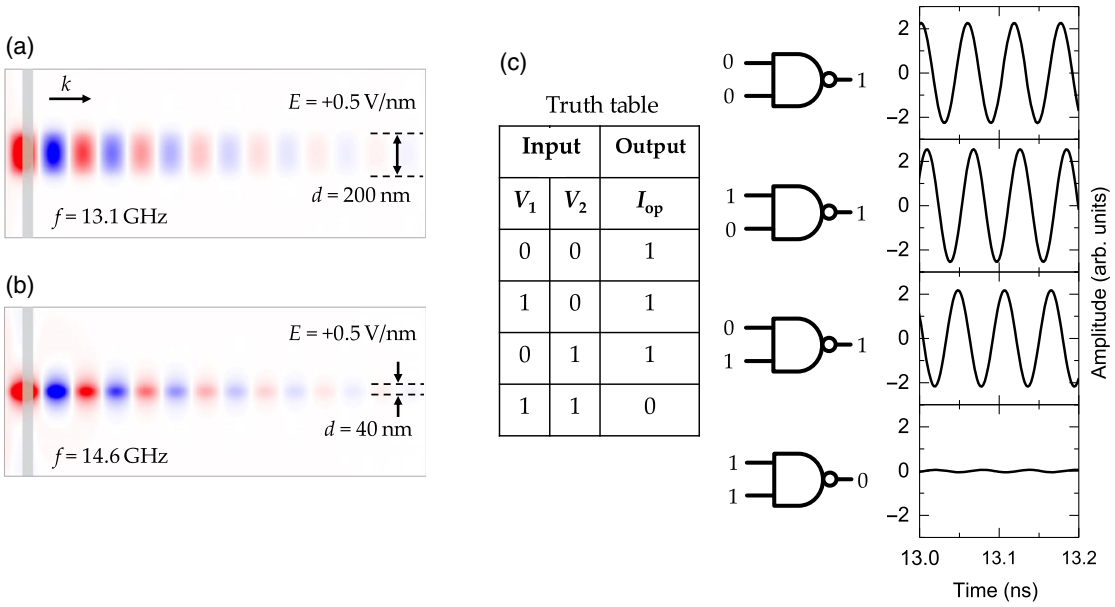

FIG. 10. (a),(b) Simulated spatial maps of dynamic magnetization show SW confinement in the 200- and 40-nm straight channel by VCMA in the absence of the bias magnetic field. (c) Simulated results show the operation of a voltage-controlled universal NAND gate in the absence of the bias magnetic field. The model device structure for the NAND gate is same as shown in Fig. 7(a).

One of the main concerns about the magnonic devices is to decrease the power consumption. This can be done to some extent by exciting SWs by VCMA [59,66,67]. However, one of the main sources of power consumption is the bias magnetic field, which needs a continuous supply of power. We also use a 50-mT bias magnetic field along an out-of-plane direction for our simulations. However, sufficiently strong PMA of ultrathin ferromagnetic films are able to align the magnetization along the out-of-plane direction even in the absence of an external bias magnetic field. Therefore, all the functionalities of magnonic devices, discussed in this paper, should be unaffected even after removing the bias magnetic field. We perform some additional micromagnetic simulations to confirm that the NCs logic devices can even be functioning in the absence of the bias magnetic field. In Fig. 10, we demonstrate some examples of simulated results on this. It shows that the NCs down to a few tens of nanometers and the universal NAND gate can be configured by VCMA even in the absence of the bias magnetic field for ultrathin ferromagnetic film with a large interfacial PMA. These results will motivate further experimental studies for the development of all-voltage-controlled low-power magnonic devices.

ACKNOWLEDGMENTS

This work is supported by a Grant-in-Aid for Scientific Research on Innovative Area, "Nano Spin Conversion Science" (Grant No. 26103002).

APPENDIX A: SPIN-WAVE (SW) FREQUENCY VERSUS CHANNEL WIDTH

See Fig. 11.

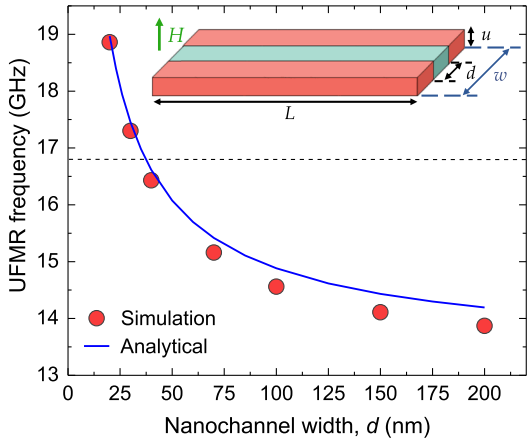

FIG. 11. The frequency of the uniform ferromagnetic resonance (UFMR) is plotted as a function of nanochannel (NC) width (d) for $E = +0.5$ V/nm (considering $\beta = 155$ fJ/Vm). The solid line is the analytical curve, plotted by using Eq. (1). The demagnetizing factors are calculated by using Refs. [63, 64]. The dotted line shows the frequency corresponds to UFMR for a waveguide with $w = 800$ nm, $E = 0$ V/nm. It shows that the UFMR frequency increases monotonically with the decrease of d and the UFMR frequency of a NC with $d \approx 35$ nm, $E = +0.5$ V/nm becomes equal to the UFMR frequency of a WG with $w = 800$ nm, $E = 0$ V/nm. Therefore, the SWs cannot be confined within a NC with width $d < 40$ nm by applying $E = +0.5$ V/nm.

APPENDIX B: SW CONFINEMENT AT A LOWER VALUE OF APPLIED ELECTRIC FIELD

See Fig. 12.

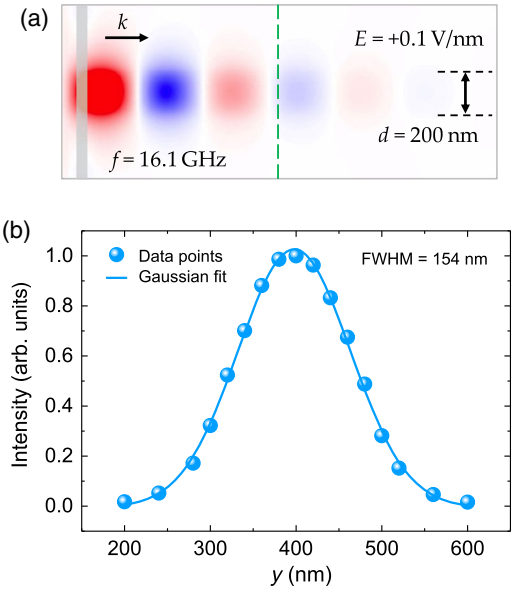

FIG. 12. (a) The snapshot of dynamic magnetization shows the SW confinement in a 200-nm channel by applying $E = +0.1$ V/nm. (b) The graph shows the line scan of the SW intensity at $x = 1$ μm along the dotted green line in part (a). The solid line is the fitting with a Gaussian function. The full width at half maxima (FWHM) is found to be 154 nm from the fitting. It shows that the SW can be strongly confined within the 200-nm channel even by applying $E = +0.1$ V/nm.

APPENDIX C: DIFFERENT CONFIGURATIONS OF THE SPIN-WAVE NANOCHANNEL (SWNC) BY VOLTAGE-CONTROLLED MAGNETIC ANISOTROPY (VCMA)

See Fig. 13.

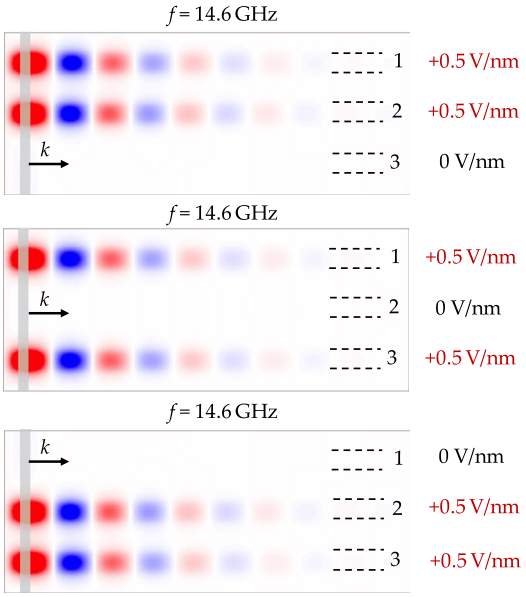

FIG. 13. In Fig. 5, we show the different configurations of three parallel NC with a width of $d = 100$ nm. Here, we show some more examples of NC configuration for SW propagation. The spatial maps of dynamic magnetization show that any combination of two NCs can be selected for sending propagating SWs by selectively applying VCMA.

APPENDIX D: INCREASE OF WAVE VECTOR (k_x) UNDER THE APPLICATION OF THE POSITIVE GATE VOLTAGE

See Fig. 14.

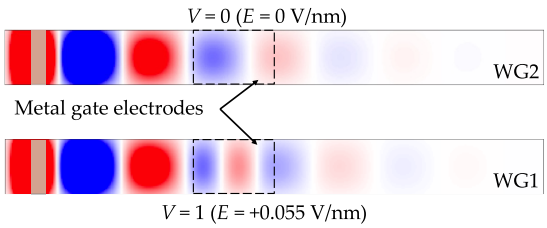

FIG. 14. This snapshot of dynamic magnetization represents the decrease of the SW wavelength (λ), i.e., the increase of the wave vector (k_x) underneath the metal gate electrode when the positive gate voltage is applied. It also shows that the SW accumulates π more phase when $E = +0.055$ V/nm is applied (in WG1) as compared to the SW phase when $E = 0$ V/nm is applied (in WG2).

APPENDIX E: SW DECAY LENGTH WITH WAVE VECTOR (k_x)

See Fig. 15.

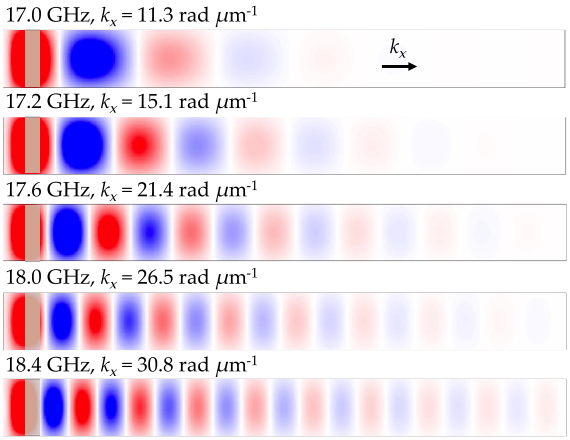

FIG. 15. The snapshots of dynamic magnetizations are shown at different values of excitation frequencies (f) and wave vectors (k_x). It shows that the SW travels a longer distance, i.e., the SW decay length increases with the increase of f or k_x. The reason behind this is the increase of the SW group velocity $[v_g = 2\pi(df/dk_x)]$ with k_x. The group velocity v_g can be calculated either from an analytical expression (described in Appendix F) or from the slope of the simulated f versus k_x curve in Fig. 1(c). The analytical expression shows that v_g is roughly proportional to k_x; Fig. 1(c) also shows that the slope of dispersion curve, i.e., v_g increases gradually with the increase of k_x.

APPENDIX F: EXPRESSION FOR GROUP VELOCITY (v_g)

$$f = \frac{\gamma\mu_0}{2\pi}\left\{\left(H + \frac{2A}{\mu_0 M_s}k_x^2 + H_p(E)(N_y - N_z)M_s\right)\right.$$
$$\times\left[H + \frac{2A}{\mu_0 M_s}k_x^2 + H_p(E)\right.$$
$$\left.\left.+(N_x - N_z)M_s\left(\frac{1 - e^{-k_x u}}{k_x u}\right)\right]\right\}^{1/2}$$

$$v_g = \frac{dw}{dk_x} = 2\pi\frac{df}{dk_x} = \frac{2A\gamma}{M_s}\frac{(C_1 + C_2 + \frac{4A}{\mu_0 M_s}k_x^2)}{\sqrt{(C_1 + \frac{2A}{\mu_0 M_s}k_x^2)(C_2 + \frac{2A}{\mu_0 M_s}k_x^2)}}k_x,$$

i.e., $v_g \propto k_x$ (v_g is roughly proportional to k_x), where $C_1 = H + H_p(E) + (N_y - N_z)M_s$ and $C_2 = H + H_p(E)$. Here, v_g is calculated by neglecting the term $(N_x - N_z)M_s$ $[(1 - e^{-k_x u})/k_x u]$, as the variation of this term with k_x is much smaller than the other terms.

[1] R. L. Stamps, S. Breitkreutz, J. Åkerman, A. V. Chumak, Y. Otani, G. E. W. Bauer, J.-U. Thiele, M. Bowen, S. A. Majetich, M. Kläui, I. L. Prejbeanu, B. Dieny, N. M. Dempsey, and B. Hillebrands, The 2014 magnetism roadmap, J. Phys. D **47**, 333001 (2014).

[2] A. V. Chumak, V. I. Vasyuchka, A. A. Serga, and B. Hillebrands, Magnon spintronics, Nat. Phys. **11**, 453 (2015).

[3] B. Lenk, H. Ulrichs, F. Garbs, and M. Münzenberg, The building blocks of magnonics, Phys. Rep. **507**, 107 (2011).

[4] T. Valet and A. Fert, Theory of the perpendicular magnetoresistance in magnetic multilayers, Phys. Rev. B **48**, 7099 (1993).

[5] S. Takahashi and S. Maekawa, Spin current in metals and superconductors, J. Phys. Soc. Jpn. **77**, 031009 (2008).

[6] B. Rana and A. Barman, Magneto-optical measurements of collective spin dynamics of two-dimensional arrays of ferromagnetic nanoelements, Spin **03**, 1330001 (2013).

[7] B. Rana, D. Kumar, S. Barman, S. Pal, Y. Fukuma, Y. Otani, and A. Barman, Detection of picosecond magnetization dynamics of 50 nm magnetic dots down to the single dot regime, ACS Nano **5**, 9559 (2011).

[8] B. Rana, D. Kumar, S. Barman, S. Pal, R. Mandal, Y. Fukuma, Y. Otani, S. Sugimoto, and A. Barman, Anisotropy in collective precessional dynamics in arrays of $Ni_{80}Fe_{20}$ nanoelements, J. Appl. Phys. **111**, 07D503 (2012).

[9] A. Haldar, D. Kumar, and A. O. Adeyeye, A reconfigurable waveguide for energy-efficient transmission and local manipulation of information in a nanomagnetic device, Nat. Nanotechnol. **11**, 437 (2016).

[10] V. Vlaminck and M. Bailleul, Spin-wave transduction at the submicrometer scale: Experiment and modeling, Phys. Rev. B **81**, 014425 (2010).

[11] M. Bailleul, D. Olligs, and C. Fermon, Propagating spin wave spectroscopy in a permalloy film: A quantitative analysis, Appl. Phys. Lett. **83**, 972 (2003).
[12] M. Madami, S. Bonetti, G. Consolo, S. Tacchi, G. Carlotti, G. Gubbiotti, F. B. Mancoff, M. A. Yar, and J. Akerman, Direct observation of a propagating spin wave induced by spin-transfer torque, Nat. Nanotechnol. **6**, 635 (2011).
[13] Y. Kajiwara, K. Harii, S. Takahashi, J. Ohe, K. Uchida, M. Mizuguchi, H. Umezawa, H. Kawai, K. Ando, K. Takanashi, S. Maekawa, and E. Saitoh, Transmission of electrical signals by spin-wave interconversion in a magnetic insulator, Nature (London) **464**, 262 (2010).
[14] H. Yu, O. d'Allivy Kelly, V. Cros, R. Bernard, P. Bortolotti, A. Anane, F. Brandl, R. Huber, I. Stasinopoulos, and D. Grundler, Magnetic thin-film insulator with ultra-low spin wave damping for coherent nanomagnonics, Sci. Rep. **4**, 6848 (2014).
[15] B. Jack and P. P. J. William, Spin-diffusion lengths in metals and alloys, and spin-flipping at metal/metal interfaces: An experimentalist's critical review, J. Phys. Condens. Matter **19**, 183201 (2007).
[16] Y. Niimi, D. Wei, H. Idzuchi, T. Wakamura, T. Kato, and Y. Otani, Experimental Verification of Comparability between Spin-Orbit and Spin-Diffusion Lengths, Phys. Rev. Lett. **110**, 016805 (2013).
[17] V. V. Kruglyak, S. O. Demokritov, and D. Grundler, Magnonics, J. Phys. D **43**, 260301 (2010).
[18] A. V. Chumak, A. A. Serga, and B. Hillebrands, Magnonic crystals for data processing, J. Phys. D **50**, 244001 (2017).
[19] B. Rana, Y. Fukuma, K. Miura, H. Takahashi, and Y. Otani, Effect of excitation power on voltage induced local magnetization dynamics in an ultrathin CoFeB film, Sci. Rep. **7**, 2318 (2017).
[20] O. Rousseau, B. Rana, R. Anami, M. Yamada, K. Miura, S. Ogawa, and Y. Otani, Realization of a micrometre-scale spin-wave interferometer, Sci. Rep. **5**, 9873 (2015).
[21] C. Banerjee, L. M. Loong, S. Srivastava, S. Pal, X. Qiu, H. Yang, and A. Barman, Improvement of chemical ordering and magnetization dynamics of Co-Fe-Al-Si Heusler alloy thin films by changing adjacent layers, RSC Adv. **6**, 77811 (2016).
[22] S. Pan, S. Mondal, T. Seki, K. Takanashi, and A. Barman, Influence of thickness-dependent structural evolution on ultrafast magnetization dynamics in $Co_2Fe_{0.4}Mn_{0.6}Si$ Heusler alloy thin films, Phys. Rev. B **94**, 184417 (2016).
[23] V. Lauer, D. A. Bozhko, T. Brächer, P. Pirro, V. I. Vasyuchka, A. A. Serga, M. B. Jungfleisch, M. Agrawal, Y. V. Kobljanskyj, G. A. Melkov, C. Dubs, B. Hillebrands, and A. V. Chumak, Spin-transfer torque based damping control of parametrically excited spin waves in a magnetic insulator, Appl. Phys. Lett. **108**, 012402 (2016).
[24] K. Vogt, F. Y. Fradin, J. E. Pearson, T. Sebastian, S. D. Bader, B. Hillebrands, A. Hoffmann, and H. Schultheiss, Realization of a spin-wave multiplexer, Nat. Commun. **5**, 3727 (2014).
[25] V. E. Demidov, S. O. Demokritov, K. Rott, P. Krzysteczko, and G. Reiss, Nano-optics with spin waves at microwave frequencies, Appl. Phys. Lett. **92**, 232503 (2008).
[26] K. Vogt, H. Schultheiss, S. Jain, J. E. Pearson, A. Hoffmann, S. D. Bader, and B. Hillebrands, Spin waves turning a corner, Appl. Phys. Lett. **101**, 042410 (2012).
[27] S. Urazhdin, V. E. Demidov, H. Ulrichs, T. Kendziorczyk, T. Kuhn, J. Leuthold, G. Wilde, and S. O. Demokritov, Nano-magnonic devices based on the spin-transfer torque, Nat. Nanotechnol. **9**, 509 (2014).
[28] Q. Wang, A. V. Chumak, L. Jin, H. Zhang, B. Hillebrands, and Z. Zhong, Voltage-controlled nanoscale reconfigurable magnonic crystal, Phys. Rev. B **95**, 134433 (2017).
[29] A. Khitun, M. Bao, and K. L. Wang, Spin wave magnetic nanofabric: A new approach to spin-based logic circuitry, IEEE Trans. Magn. **44**, 2141 (2008).
[30] V. E. Demidov, J. Jersch, S. O. Demokritov, K. Rott, P. Krzysteczko, and G. Reiss, Transformation of propagating spin-wave modes in microscopic waveguides with variable width, Phys. Rev. B **79**, 054417 (2009).
[31] B. K. Mahato, B. Rana, R. Mandal, D. Kumar, S. Barman, Y. Fukuma, Y. Otani, and A. Barman, Configurational anisotropic spin waves in cross-shaped $Ni_{80}Fe_{20}$ nanoelements, Appl. Phys. Lett. **102**, 192402 (2013).
[32] F. Heussner, A. A. Serga, T. Brächer, B. Hillebrands, and P. Pirro, A switchable spin-wave signal splitter for magnonic networks, Appl. Phys. Lett. **111**, 122401 (2017).
[33] V. E. Demidov, S. O. Demokritov, D. Birt, B. O'Gorman, M. Tsoi, and X. Li, Radiation of spin waves from the open end of a microscopic magnetic-film waveguide, Phys. Rev. B **80**, 014429 (2009).
[34] T. Schneider, A. A. Serga, A. V. Chumak, C. W. Sandweg, S. Trudel, S. Wolff, M. P. Kostylev, V. S. Tiberkevich, A. N. Slavin, and B. Hillebrands, Nondiffractive Subwavelength Wave Beams in a Medium with Externally Controlled Anisotropy, Phys. Rev. Lett. **104**, 197203 (2010).
[35] T. Sebastian, T. Brächer, P. Pirro, A. A. Serga, B. Hillebrands, T. Kubota, H. Naganuma, M. Oogane, and Y. Ando, Nonlinear Emission of Spin-Wave Caustics from an Edge Mode of a Microstructured $Co_2Mn_{0.6}Fe_{0.4}Si$ Waveguide, Phys. Rev. Lett. **110**, 067201 (2013).
[36] F. Garcia-Sanchez, P. Borys, R. Soucaille, J.-P. Adam, R. L. Stamps, and J.-V. Kim, Narrow Magnonic Waveguides Based on Domain Walls, Phys. Rev. Lett. **114**, 247206 (2015).
[37] K. Wagner, A. Kákay, K. Schultheiss, A. Henschke, T. Sebastian, and H. Schultheiss, Magnetic domain walls as reconfigurable spin-wave nanochannels, Nat. Nanotechnol. **11**, 432 (2016).
[38] K. Alexander, B. Mingqiang, and L. W. Kang, Magnonic logic circuits, J. Phys. D **43**, 264005 (2010).
[39] D. Grundler, Reconfigurable magnonics heats up, Nat. Phys. **11**, 438 (2015).
[40] K. Miura, S. Yabuuchi, M. Yamada, M. Ichimura, B. Rana, S. Ogawa, H. Takahashi, Y. Fukuma, and Y. Otani, Voltage-induced magnetization dynamics in CoFeB/MgO/CoFeB magnetic tunnel junctions, Sci. Rep. **7**, 42511 (2017).
[41] T. Maruyama, Y. Shiota, T. Nozaki, K. Ohta, N. Toda, M. Mizuguchi, A. A. Tulapurkar, T. Shinjo, M. Shiraishi, S. Mizukami, Y. Ando, and Y. Suzuki, Large voltage-induced magnetic anisotropy change in a few atomic layers of iron, Nat. Nanotechnol. **4**, 158 (2009).

[42] S.-S. Ha, N.-H. Kim, S. Lee, C.-Y. You, Y. Shiota, T. Maruyama, T. Nozaki, and Y. Suzuki, Voltage induced magnetic anisotropy change in ultrathin $Fe_{80}Co_{20}$/MgO junctions with Brillouin light scattering, Appl. Phys. Lett. **96**, 142512 (2010).

[43] T. Schneider, A. A. Serga, B. Leven, B. Hillebrands, R. L. Stamps, and M. P. Kostylev, Realization of spin-wave logic gates, Appl. Phys. Lett. **92**, 022505 (2008).

[44] N. Sato, K. Sekiguchi, and Y. Nozaki, Electrical demonstration of spin-wave logic operation, Appl. Phys. Express **6**, 063001 (2013).

[45] K.-S. Lee and S.-K. Kim, Conceptual design of spin wave logic gates based on a Mach-Zehnder-type spin wave interferometer for universal logic functions, J. Appl. Phys. **104**, 053909 (2008).

[46] S. Klingler, P. Pirro, T. Brächer, B. Leven, B. Hillebrands, and A. V. Chumak, Spin-wave logic devices based on isotropic forward volume magnetostatic waves, Appl. Phys. Lett. **106**, 212406 (2015).

[47] M. P. Kostylev, A. A. Serga, T. Schneider, B. Leven, and B. Hillebrands, Spin-wave logical gates, Appl. Phys. Lett. **87**, 153501 (2005).

[48] M. J. Donahue and D. G. Porter, OOMMF User's Guide, Version 1.0, Interagency Report NISTIR 6376, National Institute of Standards and Technology, Gaithersburg, MD, 1999 [http://math.nist.gov/oommf/].

[49] S. Ikeda, K. Miura, H. Yamamoto, K. Mizunuma, H. D. Gan, M. Endo, S. Kanai, J. Hayakawa, F. Matsukura, and H. Ohno, A perpendicular-anisotropy CoFeB-MgO magnetic tunnel junction, Nat. Mater. **9**, 721 (2010).

[50] Y. Shiota, F. Bonell, S. Miwa, N. Mizuochi, T. Shinjo, and Y. Suzuki, Opposite signs of voltage-induced perpendicular magnetic anisotropy change in CoFeBMgO junctions with different underlayers, Appl. Phys. Lett. **103**, 082410 (2013).

[51] Y. Shiota, S. Murakami, F. Bonell, T. Nozaki, T. Shinjo, and Y. Suzuki, Quantitative evaluation of voltage-induced magnetic anisotropy change by magnetoresistance measurement, Appl. Phys. Express **4**, 043005 (2011).

[52] T. Nozaki, Y. Kay, T. Shingo, S. Masaki, M. Rie, K. Makoto, K. Hitoshi, F. Akio, and Y. Shinji, Voltage-induced magnetic anisotropy changes in an ultrathin FeB layer sandwiched between two MgO layers, Appl. Phys. Express **6**, 073005 (2013).

[53] X. Li, K. Fitzell, D. Wu, C. T. Karaba, A. Buditama, G. Yu, K. L. Wong, N. Altieri, C. Grezes, N. Kioussis, S. Tolbert, Z. Zhang, J. P. Chang, P. K. Amiri, and K. L. Wang, Enhancement of voltage-controlled magnetic anisotropy through precise control of Mg insertion thickness at CoFeBMgO interface, Appl. Phys. Lett. **110**, 052401 (2017).

[54] A. Okada, S. Kanai, M. Yamanouchi, S. Ikeda, F. Matsukura, and H. Ohno, Electric-field effects on magnetic anisotropy and damping constant in Ta/CoFeB/MgO investigated by ferromagnetic resonance, Appl. Phys. Lett. **105**, 052415 (2014).

[55] S. Miwa, M. Suzuki, M. Tsujikawa, K. Matsuda, T. Nozaki, K. Tanaka, T. Tsukahara, K. Nawaoka, M. Goto, Y. Kotani, T. Ohkubo, F. Bonell, E. Tamura, K. Hono, T. Nakamura, M. Shirai, S. Yuasa, and Y. Suzuki, Voltage controlled interfacial magnetism through platinum orbits, Nat. Commun. **8**, 15848 (2017).

[56] S. Miwa, J. Fujimoto, P. Risius, K. Nawaoka, M. Goto, and Y. Suzuki, Strong Bias Effect on Voltage-Driven Torque at Epitaxial Fe-MgO Interface, Phys. Rev. X **7**, 031018 (2017).

[57] A. Kozioł-Rachwał, T. Nozaki, K. Freindl, J. Korecki, S. Yuasa, and Y. Suzuki, Enhancement of perpendicular magnetic anisotropy and its electric field-induced change through interface engineering in Cr/Fe/MgO, Sci. Rep. **7**, 5993 (2017).

[58] F. Bonell, S. Murakami, Y. Shiota, T. Nozaki, T. Shinjo, and Y. Suzuki, Large change in perpendicular magnetic anisotropy induced by an electric field in FePd ultrathin films, Appl. Phys. Lett. **98**, 232510 (2011).

[59] B. Rana, Y. Fukuma, K. Miura, H. Takahashi, and Y. Otani, Excitation of coherent propagating spin waves in ultrathin CoFeB film by voltage-controlled magnetic anisotropy, Appl. Phys. Lett. **111**, 052404 (2017).

[60] K. Nawaoka, S. Miwa, Y. Shiota, N. Mizuochi, and Y. Suzuki, Voltage induction of interfacial Dzyaloshinskii-Moriya interaction in Au/Fe/MgO artificial multilayer, Appl. Phys. Express **8**, 063004 (2015).

[61] B. A. Kalinikos and A. N. Slavin, Theory of dipole-exchange spin wave spectrum for ferromagnetic films with mixed exchange boundary conditions, J. Phys. C **19**, 7013 (1986).

[62] S. O. Demokritov, B. Hillebrands, and A. N. Slavin, Brillouin light scattering studies of confined spin waves: Linear and nonlinear confinement, Phys. Rep. **348**, 441 (2001).

[63] M. Sato and Y. Ishii, Simple and approximate expressions of demagnetizing factors of uniformly magnetized rectangular rod and cylinder, J. Appl. Phys. **66**, 983 (1989).

[64] A. Aharoni, Demagnetizing factors for rectangular ferromagnetic prisms, J. Appl. Phys. **83**, 3432 (1998).

[65] A. Barman, S. Wang, J. D. Maas, A. R. Hawkins, S. Kwon, A. Liddle, J. Bokor, and H. Schmidt, Magneto-optical observation of picosecond dynamics of single nanomagnets, Nano Lett. **6**, 2939 (2006).

[66] T. Nozaki, Y. Shiota, S. Miwa, S. Murakami, F. Bonell, S. Ishibashi, H. Kubota, K. Yakushiji, T. Saruya, A. Fukushima, S. Yuasa, T. Shinjo, and Y. Suzuki, Electric-field-induced ferromagnetic resonance excitation in an ultrathin ferromagnetic metal layer, Nat. Phys. **8**, 491 (2012).

[67] R. Verba, V. Tiberkevich, I. Krivorotov, and A. Slavin, Parametric Excitation of Spin Waves by Voltage-Controlled Magnetic Anisotropy, Phys. Rev. Applied **1**, 044006 (2014).